materials

MDPI

Article

Valorization of Tomato Stems into Biochar for Efficient Adsorptive Removal of Cationic and Anionic Dyes from Aqueous Solutions

Beata Doczekalska [1,*], Krzysztof Kuśmierek [2] and Andrzej Świątkowski [2]

[1] Faculty of Forestry and Wood Technology, Department of Chemical Wood Technology, Poznan University of Life Sciences, 60-637 Poznan, Poland
[2] Faculty of Advanced Technologies and Chemistry, Institute of Chemistry, Military University of Technology, 00-908 Warsaw, Poland; krzysztof.kusmierek@wat.edu.pl (K.K.); a.swiatkowski@wp.pl (A.Ś.)
* Correspondence: beata.doczekalska@up.poznan.pl; Tel.: +48-61-8487463

Abstract

The biochars obtained by pyrolyzing tomato stems at temperatures of 400, 500, 600, and 700 °C were characterized, and their ability to absorb anionic (Direct Orange 26, DO26) and cationic (Rhodamine B, RhB) dyes from aqueous solutions was investigated. The effects of solution pH and ionic strength were studied. It was found that the adsorption process of both dyes was pH-dependent, but no effect of ionic strength was observed. The kinetics of dye adsorption on biochars were well described by the pseudo-second-order model. The equilibrium adsorption data were analyzed using the Freundlich, Langmuir, and Temkin isotherms. All three equations described dye adsorption on biochars quite well, although a slightly better fit was observed for the Freundlich model. The maximum adsorption capacities of BCs ranged from 54.44 mg/g (BC400) to 108.1 mg/g (BC700) for DO26 and from 4.483 mg/g (BC700) to 8.887 mg/g (BC400) for RhB. The study reveals that biochars derived from tomato stems can be used as efficient, low-cost adsorbents for the removal of anionic and cationic dyes from water.

Keywords: adsorption; biochar; tomato stems; Direct Orange 26; Rhodamine B

1. Introduction

Water contamination caused by synthetic dyes is a growing environmental issue worldwide. Dyes are extensively used in the textile, paper, plastic, and food industries, and a considerable portion of these compounds is discharged into aquatic ecosystems without adequate treatment. Due to their complex aromatic structures, dyes are generally resistant to biodegradation, photolysis, and oxidation, resulting in their long-term persistence in water bodies [1]. Among these dyes, Rhodamine B (RhB) and Direct Orange 26 (DO26) are particularly problematic. RhB, a cationic xanthene dye, is toxic, mutagenic, and capable of bioaccumulation, whereas DO26, an anionic azo dye, exhibits strong color stability but potential carcinogenicity. Even in minimal concentrations, both dyes diminish light penetration, impede photosynthesis, and disrupt aquatic ecosystems [2].

Traditional wastewater treatment methods, such as coagulation, flocculation, membrane filtration, and advanced oxidation processes, are often limited by high operational costs, complex maintenance, and incomplete dye degradation. In contrast, adsorption has been recognized as one of the most economical and effective techniques for dye removal due to its simplicity, the reusability of materials, and high pollutant removal efficiency [3].

Academic Editors: Chun Yang Yin and Carlos Javier Duran-Valle

Received: 22 December 2025
Revised: 3 February 2026
Accepted: 19 February 2026
Published: 26 February 2026

The search for sustainable, low-cost adsorbents derived from natural or waste materials has therefore become a key area of environmental research.

Biochar is a carbon-rich, porous material obtained through the thermochemical conversion (typically pyrolysis) of biomass under limited oxygen conditions and has emerged as a promising adsorbent for the remediation of contaminated water and soil [4–6]. Its physicochemical characteristics—such as specific surface area, pore structure, surface functionality, and aromaticity—depend strongly on the feedstock composition and pyrolysis parameters (temperature, heating rate, and residence time). The presence of abundant oxygen-containing functional groups (–COOH, –OH, –C=O) enables electrostatic interactions, hydrogen bonding, and π–π electron donor–acceptor interactions with dye molecules [1]. Consequently, biochars produced from a variety of agricultural and forestry residues—such as rice husks, corn stalks, sugarcane bagasse, sawdust, and fruit peels—have shown remarkable performance in removing both cationic and anionic dyes from aqueous solutions [7].

The use of biomass residues for biochar production offers multiple environmental and economic benefits. It transforms low-value agricultural by-products into functional materials, reduces waste management problems, and supports circular economy principles [8]. Moreover, biochar production contributes to carbon sequestration, thereby mitigating greenhouse gas emissions and promoting climate sustainability [9]. When compared with conventional activated carbon, biochar offers lower production costs, renewability, and the potential for surface modification to enhance its adsorption capacity [10]. These attributes make biochar a promising alternative adsorbent for applications involving large-scale wastewater treatment [11]. Review studies have further highlighted biochar as an eco-friendly and economical adsorbent for the removal of toxic cationic and anionic dyes from aqueous environments [3,12].

Tomato (*Solanum lycopersicum*) cultivation generates substantial quantities of agricultural residues, including stems and leaves, which are often discarded or incinerated after harvest, leading to environmental pollution and the loss of valuable organic carbon. Based on the research conducted by Drecher and co-workers [13], it has been found that the vegetative residues of tomato plants contain a wide range of biologically active compounds. Tomato stems are rich in lignocellulosic components (cellulose, hemicellulose, and lignin), making them a suitable precursor for producing biochar [14]. Previous studies have explored the valorization of tomato stem biomass for materials engineering, for example, as biochar fillers in biodegradable composites [15,16] and, more recently, as adsorbents for inorganic ions or anionic dyes such as Direct Orange 46 [2]. However, studies combining both cationic and anionic dye removal using biochar derived specifically from tomato stems remain limited.

The main aim of this study is to valorize tomato stem waste through its conversion into biochar and to evaluate its potential as a sustainable and cost-effective adsorbent for removing dyes from aqueous solutions. To this end, biochar derived from tomato stems was produced and characterized, and its adsorption performance toward a cationic dye (Rhodamine B) and an anionic dye (Direct Orange 26) was systematically investigated. The effects of initial dye concentration, solution pH, and ionic strength were assessed, and adsorption kinetics and equilibrium isotherms were analyzed to elucidate the underlying adsorption mechanisms.

2. Materials and Methods

2.1. Reagents and Materials

The Rhodamine B (RhB) cationic dye (≥95%) was received from Sigma-Aldrich (Darmstadt, Germany), while the Direct Orange 26 (DO26) anionic azo dye was obtained from Boruta-Zachem SA (Bydgoszcz, Poland). The most important information about both

dyes is listed in Table 1. The other high-purity chemicals and reagents were purchased from Chempur (Piekary Śląskie, Poland) or Avantor Performance Materials Poland SA (Gliwice, Poland).

Table 1. Properties of Direct Orange 26 and Rhodamine B dyes.

	Direct Orange 26	Rhodamine B
CAS Number	3626-36-6	81-88-9
λ max	492 nm	552 nm
Color Index	29,150	45,170
Molar weight	756.67 g/mol	479.02 g/mol
Formula	$C_{33}H_{22}N_6Na_2O_9S_2$	$C_{28}H_{31}ClN_2O_3$
Structure	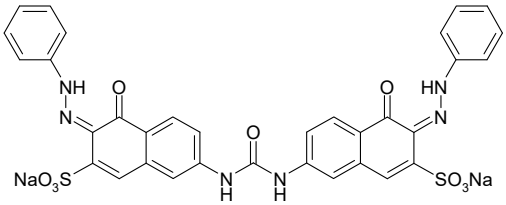	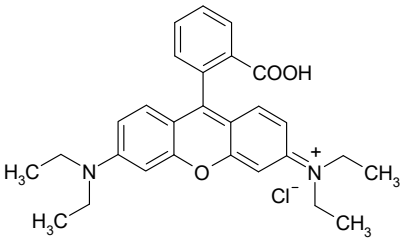
TPSA *	262 Å^2	52.8 Å^2

* Topological polar surface area.

2.2. Preparation and Characterization of the Biochars

2.2.1. Analysis of the Chemical Composition of Tomato Stems

Tomato stems used for biochar production were obtained from greenhouse cultivation at horticultural farms in west-central Poland. The chemical composition of tomato stem biomass (dry matter) was determined in accordance with the standards of the Technical Association of the Pulp and Paper Industry (TAPPI). The following components were analyzed: (I) cellulose, determined by the Seifert method using an acetylacetone–dioxane mixture [17]; (II) holocellulose, determined using sodium chlorite (TAPPI T 9 wd-75); (III) pentosans by Tollens' method using phloroglucinol (TAPPI—T 233 cm-84); (IV) lignin with concentrated sulfuric acid (TAPPI T 222 om-06); (V) substances that are soluble in organic solvents according to Soxhlet (TAPPI—T 204 cm-07); (VI) ash (TAPPI—T 211 cm-86) and (VII) the theoretical hemicellulose content, calculated as the difference between holocellulose and cellulose.

2.2.2. Carbonization

Tomato stems were cleaned and then dried until they reached a constant weight at a temperature of 105 °C. The raw material was then ground to a particle size of less than 20 mm using an SM100 mill (Retsch GmbH, Haan, Germany) to ensure process uniformity and effective heat transfer within the material. The stems were subsequently subjected to carbonization in a muffle furnace (Czylok, Jastrzębie-Zdrój, Poland) in an oxygen-free atmosphere with controlled process parameters. Carbonization was carried out at 400 °C, 500 °C, 600 °C, and 700 °C, with a heating rate of 3 °C min^{-1} and a 1 h dwell time at the target temperature. After carbonization, the yield was expressed as the mass of the final product. The percent yield was then calculated based on Equation (1):

$$Yield = \frac{w_A}{w_B} \cdot 100\% \quad (1)$$

where w_B—biochar weight (g) and w_A—dry biomass weight (g).

2.2.3. Characterization of Obtained Biochars

The biochar's surface morphology was characterized using scanning electron microscopy (SEM) coupled with energy-dispersive spectroscopy (EDS) (Zeiss EVO 10, Carl Zeiss Microscopy GmbH, Jena, Germany). The biochar samples were placed on stubs covered with carbon tape and then sputter-coated with a thin layer of gold using a Quorum Q150R Plus Coater (Quorum Technologies Ltd., Laughton, UK).

The quantitative determination of oxygen-containing acidic and basic surface groups of the biochars was performed using the Boehm titration method [18]. Biochar samples (0.25 ± 0.01 g) were weighed on an analytical balance and placed individually in 250 mL Erlenmeyer flasks. Each sample was treated with 25 mL of one of the following solutions: 0.1 mol/L NaOH, 0.1 mol/L $NaHCO_3$, 0.05 mol/L Na_2CO_3, or 0.1 mol/L HCl. The suspensions were shaken for 24 h at approximately 180 rpm and subsequently filtered. The filtrates were titrated using 0.1 mol/L HCl (for basic groups) or 0.1 mol/L NaOH (for acidic groups) with Tashiro's indicator. All measurements were carried out in triplicate. The amount of surface functional groups (A_x, mmol/g) was calculated using the following equation:

$$A_x = \frac{(V_0 - V_B)n_z 25}{N_B} \quad (2)$$

where V_0 and V_B are the volumes of HCl or NaOH solution used for the titration of the blank and the biochar sample, respectively; n_z is the concentration of the titrant (mol/L); and N_B is the mass of the biochar sample (g),

The iodine number, used to evaluate the adsorption capacity of the selected biochar samples, was determined by the redox titration method in accordance with the ASTM D4607-14 standard [19]. The iodine value (I) was calculated using the following equation:

$$I = \frac{(V_0 - V_p)c_{tio} \cdot 126.92}{M_B} \quad (3)$$

where V_0—the volume of $Na_2S_2O_3$ solution used in the blank (cm^3); V_p—the volume of $Na_2S_2O_3$ solution used in the actual determination (cm^3); c_{tio}—titer of $Na_2S_2O_3$ (mol/dm^3); M_B—mass of biochar (g); and 126.92—the mass of 0.5 moles of iodine (g).

To determine the point of zero charge (pH_{pzc}) of the materials, a series of 0.01 mol/L NaCl solutions was prepared and adjusted to the required initial pH (between 2 and 12) by adding small quantities of 0.01 mol/L HCl or NaOH. Then, 50 mg of adsorbent was added to each of the prepared 20 mL solutions and shaken for 24 h. The solutions were then filtered, and their final pH was measured. The pH_{pzc} value was determined graphically as the crossing point of the experimental line with the x-axis of the graph of ΔpH ($pH_{final} - pH_{initial}$) versus $pH_{initial}$.

The ash content of the biochars was determined following a modified ASTM D2866 procedure. Approximately 1.0 ± 0.1 g of pre-dried biochar sample was accurately weighed and placed in a crucible, which was then introduced into a cold muffle furnace. The temperature was gradually increased to 500 °C over 30 min and held constant for 30 to 50 min. Then, the temperature was increased to 650 ± 25 °C and held for 90 min. After combustion, the crucible was taken out of the furnace, allowed to cool to room temperature in a desiccator, and weighed. The ash content (A) was calculated using Equation (4):

$$A = \frac{m_2 - m_0}{m_1 - m_0} \cdot 100\% \quad (4)$$

where m_0—mass of the empty crucible (g); m_1—mass of the crucible with sample (g); and m_2—mass of the crucible with residue (g).

An elemental analysis of biochars was performed using a Vario EL Cube apparatus (Elementar Analysensysteme, Langenselbold, Germany) working in CHNS mode. The oxygen content (O wt.%) was estimated from the difference as follows: O% = 100% − (ΣC% + H% + N% + S%).

Thermogravimetric analysis (TGA) was performed using an STA 449 F5 Jupiter-QMS thermal analysis test stand (NETZSCH Group, Burlington, MA, USA) to characterize the surface chemistry of biochars. The sample (15 ± 1 mg) was heated from 25 °C to 950 °C at a rate of 10 °C/min, with a helium flow rate of 25 cm^3/min.

The nitrogen adsorption/desorption isotherm, measured at 77 K using an ASAP 2020 adsorption analyzer (Micromeritics Instrument Corp., Norcross, GA, USA), was employed to evaluate the porous structure parameters of the biochar. The biochar sample was degassed at 300 °C for 24 h prior to isotherm acquisition.

2.3. Batch Adsorption Studies

The adsorption capacities of biochars were evaluated for two dyes: the cationic dye Rhodamine B (RhB) and the anionic dye Direct Orange 26 (DO26). Equilibrium studies (adsorption isotherms), adsorption kinetics, and the effects of solution pH and ionic strength were investigated. All of these experiments were carried out at a temperature of 23 °C in glass Erlenmeyer flasks. These flasks contained 20 mL of dye solutions of the appropriate concentration, as well as 20 mg of individual biochars. Such prepared mixtures were agitated on a laboratory shaker at a constant speed of 200 rpm. After an appropriate time, the dye solutions were filtered and determined spectrophotometrically. The amounts of dye adsorbed onto the biocarbon at equilibrium (q_e) and after time t (q_t) were calculated using the following formulas:

$$q_e = \frac{(C_0 - C_e)V}{m} \quad (5)$$

$$q_t = \frac{(C_0 - C_t)V}{m} \quad (6)$$

where C_0 is the initial concentration of DO26 or RhB (μmol/L), C_t is the dye concentration measured at time t (μmol/L), C_e is the concentration of the dye at equilibrium (μmol/L), m is the mass of the biochar sample (0.02 g), and V is the volume of the solution (0.02 L).

The percentage of removal was calculated based on the following relationship:

$$\text{Removal}(\%) = \frac{(C_0 - C_e)}{C_0} \times 100 \quad (7)$$

Adsorption isotherms were studied for different initial dye concentrations, ranging from 5 to 30 μmol/L for RhB and from 20 to 70 μmol/L for DO26, respectively. Kinetic experiments and studies on the effects of pH and ionic strength were carried out using a constant initial RhB and DO26 concentration of 20 μmol/L (adsorbent dose = 1 g/L). These studies were conducted at the original pH of the solutions (~4.7 for RhB and ~6.6 for DO26). However, there are some exceptions. In studies about the effect of pH on adsorption, dye solutions (20 μmol/L) were adjusted to the desired pH in the range of 2.5–10.0. This was achieved using small amounts of 0.01 mol/L HCl and NaOH. When studying the effect of ionic strength on adsorption, an appropriate amount of NaCl was added to 20 mL of the 20 μmol/L dye solution, resulting in final salt concentrations of 0.1, 0.5, 1.0, and 2.0 mol/L. All the above adsorption experiments were performed in duplicate, and the averaged results were used for further calculations.

For the description of adsorption kinetics, two of the most popular kinetic models were employed: the pseudo-first-order (PFO) and pseudo-second-order (PSO) models. The linear forms of these models are represented by the following equations [20]:

$$\log(q_e - q_t) = \log q_e - \frac{k_1}{2.303}t \quad (8)$$

$$\frac{t}{q_t} = \frac{1}{k_2 q_e^2} + \frac{1}{q_e}t \quad (9)$$

where k_1 (1/min) and k_2 (g/μmol·min) are the PFO and the PSO adsorption rate constants, respectively.

The adsorption rate constants (k_1 and k_2) and the equilibrium adsorption capacity (q_e) values for both kinetic models were calculated from the slopes and intercepts of $\log(q_e - q_t)$ vs. t for PFO and t/q_t vs. t for PSO, respectively.

The Weber–Morris kinetic model [20,21] is expressed by the following formula:

$$q_t = k_i t^{0.5} + C_i \quad (10)$$

where k_i—intraparticle diffusion rate constant (μmol/g·min$^{-0.5}$) and C_i—constant of the Weber–Morris equation.

For the description of the experimental adsorption isotherms, the Freundlich, Langmuir, and Temkin isotherm models were used [22]:

$$q_e = K_F C_e^{1/n} \quad (11)$$

$$q_e = \frac{q_m K_L C_e}{1 + K_L C_e} \quad (12)$$

$$q_e = \frac{RT}{b_T}\ln(A_T C_e) \quad (13)$$

After conversion to linear form, these formulas are as follows:

$$\ln q_e = \ln K_F + \frac{1}{n}\ln C_e \quad (14)$$

$$\frac{C_e}{q_e} = \frac{1}{q_m}C_e + \frac{1}{q_m K_L} \quad (15)$$

$$q_e = \frac{RT}{b_T}\ln A_T + \left(\frac{RT}{b_T}\right)\ln C_e \quad (16)$$

where K_F is the Freundlich isotherm constant giving the relative adsorption capacity of the adsorbent ((μmol/g)·(L/μmol)$^{1/n}$), n is the Freundlich constant, q_m is the Langmuir's maximum adsorption capacity (μmol/g), K_L is the Langmuir constant (L/μmol), A_T (L/g) and b_T (J/mol) are the Temkin isotherm constants, T is the temperature (K), and R is the gas constant (8.314 J/mol·K).

The constant isotherms were determined based on the slope and intercept obtained for the linear plots of $\ln q_e$ vs. $\ln C_e$ (Freundlich), C_e/q_e vs. C_e (Langmuir), and q_e vs. $\ln C_e$ (Temkin).

To assess the fit of the model to the experimental data, the determination coefficients (R^2), chi-square (χ^2), and root mean squared error (RMSE) were used. A higher R^2 (closer

to 1) as well as lower values of χ^2 and RMSE indicate a better fit of the model. These parameters were calculated as follows:

$$R^2 = \frac{\sum_{i=1}^{n}\left(q_{e(\mathrm{cal})} - \overline{q_{e(\mathrm{exp})}}\right)^2}{\sum_{i=1}^{n}\left(q_{e(\mathrm{cal})} - \overline{q_{e(\mathrm{exp})}}\right)^2 + \sum_{i=1}^{n}\left(q_{e(\mathrm{cal})} - q_{e(\mathrm{exp})}\right)^2} \quad (17)$$

$$\chi^2 = \sum_{i=1}^{n} \frac{\left(q_{e(\mathrm{exp})} - q_{e(\mathrm{cal})}\right)^2}{q_{e(\mathrm{cal})}} \quad (18)$$

$$\mathrm{RMSE} = \sqrt{\frac{1}{\mathrm{n}}\sum_{\mathrm{i}=1}^{\mathrm{n}}\left(q_{\mathrm{e(exp)}} - q_{\mathrm{e(cal)}}\right)^2} \quad (19)$$

where $q_{\mathrm{e(exp)}}$ and $q_{\mathrm{e(cal)}}$ are the adsorption capacities (μmol/g) obtained experimentally and calculated from the kinetic or isotherm model, respectively.

The dye concentrations in the solutions used in all adsorption experiments were determined spectrophotometrically using a Varian Cary 3E series spectrophotometer (Palo Alto, CA, USA). Absorbance was measured at analytical wavelengths of 492 nm (DO26) and 552 nm (RhB), which correspond to the absorption maxima of the respective dyes. The calibration curve for the determination of DO26 was linear (R^2 = 0.999) within the tested concentration range of 5–60 μmol/L and was described by the equation $y = 0.0195x + 0.0186$. The correlation of the RhB absorbances versus concentration (1–25 μmol/L) was described by the equation $y = 0.0946x + 0.0154$, with a coefficient of determination equal to 0.998.

3. Results and Discussion

3.1. Properties of the Obtained Tomato Stem-Derived Biochars (BCs-(400–700))

The chemical composition analysis of tomato stems revealed that the material contained 39.42% cellulose, 17.47% lignin, 19.30% pentosans, 69.95% holocellulose, 30.53% hemicellulose, 13.40% ash, and 10.60% extractives. In comparison, Tiryaki et al. [14] reported the content of the main components in tomato stems as 27.03% cellulose, 16.01% lignin, 21.08% hemicellulose, 10.65% ash, and 21.65% unidentified substances. Differences in chemical composition may result from varying environmental conditions, including soil type, fertilization practices, mineral content in the substrate, and climatic factors during the growing season. The higher ash content observed in this study (13.40% compared to 10.65%) may indicate a greater accumulation of mineral substances in plant tissues, which is characteristic of biomass derived from soils rich in mineral salts or from intensively fertilized cultivation sites.

When compared with woody biomass (softwood and hardwood) (Table 2), tomato stems show a similar cellulose content (around 40%) but a significantly higher ash content, reflecting the greater accumulation of mineral components typical of herbaceous plants. In relation to other lignocellulosic materials, such as wheat straw and *Miscanthus giganteus*, tomato stems exhibit comparable cellulose and lignin contents but a notably higher ash level. In contrast, rice husks are characterized by an exceptionally high mineral content (approximately 18.7%), mainly due to the presence of large amounts of silica in their structure. In summary, the obtained results confirm that tomato stems possess a chemical composition similar to other lignocellulosic materials and can be considered a promising feedstock for thermochemical conversion processes, including biochar production.

Table 2. Chemical composition of selected lignocellulosic materials.

Material	Cellulose	Hemicellulose	Lignin	Ash	Ref.
			(wt.%)		
Tomato stems	39.42	30.53	17.47	13.40	this study
Softwood	40–45	25–30	25–30	0.2–1.0	[23,24]
Hardwood	40–50	25–35	20–25	0.5–2.0	[23,25]
Miscanthus giganteus	45.12	29.30	22.21	2.63	[26]
Wheat straw	37.80	28.20	19.80	3.70	[27]
Rice husks	36.50	23.50	19.30	18.70	[28]

Conducted analyses showed that the yield of tomato stem carbonization decreased with increasing process temperature. At 400 °C, the yield was 38.6%, while at 500 °C, it declined to 37.9%. Raising the temperature to 600 °C resulted in a further decrease in yield to 35.9%, and at 700 °C, the yield reached 34.1%. The obtained results indicate that higher process temperatures intensify biomass thermolysis reactions, leading to a reduction in the amount of biochar produced.

The elemental composition of the biochar was determined using two instrumental techniques: SEM–EDS and CHNS elemental analysis. SEM–EDS reflects the elemental composition of the surface layer of the material, while CHNS analysis determines its total mass composition.

SEM images of the obtained biochars show morphological differences resulting from the carbonization process temperature. Figure 1 shows representative SEM images of biochars produced at two different temperatures. A visual comparison indicates that higher-temperature thermal treatment results in smaller biocarbon particles. For BC400, particles larger than 15 µm are visible, whereas for BC700, particles smaller than 8 µm dominate. These values are approximate and are used only to illustrate the qualitative morphological trends observed, and they do not constitute a quantitative analysis of particle size.

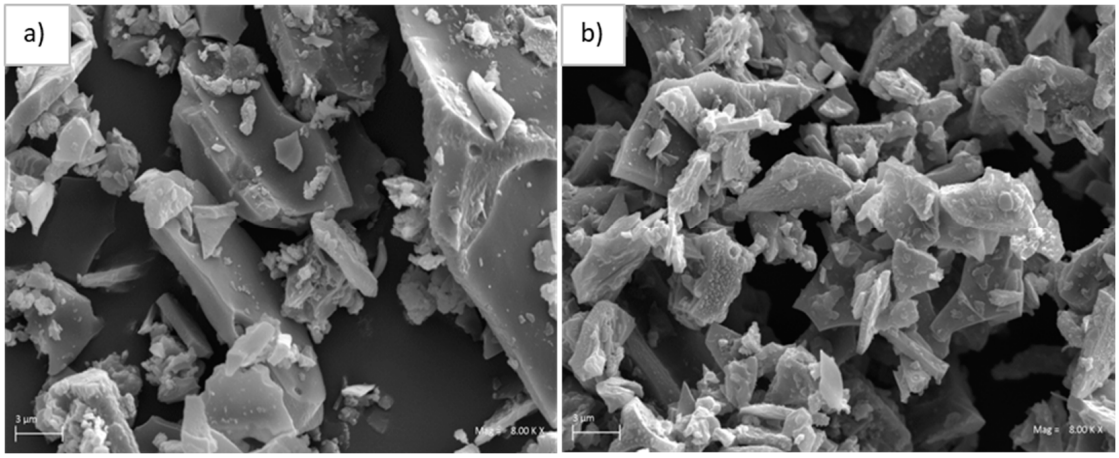

Figure 1. The SEM images of biochar samples: (**a**) BC400 and (**b**) BC700 (magnification 8000×).

An SEM–EDS analysis was performed to characterize the surface chemistry of biochars. The determined percentage content of elements is presented in Table 3. As can be seen, the C and O contents decrease with increasing temperature, whereas the contents of K, Cl, Ca, P, and S increase. This behavior can be attributed to mass loss during pyrolysis, accompanied by the release of volatile organic compounds and gases, leading to a relative enrichment of inorganic elements on the biochar surface.

Table 3. Surface chemical composition of biochars determined by the SEM-EDS method.

Sample	Chemical Composition (wt.%)									
	C	O	K	Cl	Ca	P	S	Si	Mg	Na
BC400	83.1	12.6	2.6	0.2	0.6	0.3	0.1	0.1	0.2	0.2
BC500	81.1	11.7	4.6	0.4	0.8	0.5	0.2	0.1	0.2	0.2
BC600	79.9	12.8	4.1	0.4	1.3	0.5	0.2	0.2	0.2	0.2
BC700	77.2	11.4	7.6	1.0	1.2	0.7	0.3	0.2	0.3	0.2

The results of the elemental analysis are listed in Table 4. As the pyrolysis temperature increases from 400 to 700 °C, the percentage content of carbon, nitrogen, and sulfur also increases. At the same time, the oxygen content gradually decreases. This trend, along with the proportions of the individual elements observed, is consistent with the results obtained in other studies [16,29]. For instance, biochar produced at 500 °C for 4 h in a N_2 atmosphere was found to consist of C 61.93%, H 2.38%, N 2.21%, and O 33.48% [16].

Table 4. Elemental analysis of tomato stem-derived biochars.

Sample	Elemental Analysis (wt.%)				
	C	H	N	S	O *
BC400	58.2	2.9	2.7	2.2	34.0
BC500	60.2	2.5	3.2	3.5	30.7
BC600	61.8	2.2	3.5	4.0	28.5
BC700	65.9	1.9	3.9	4.9	23.4

* Calculated value.

Thermogravimetric analysis (TG) of the biochars was performed over a temperature range of 35 to 950 °C. As the TG curves were similar for all the samples tested, the results are presented in tabular form (Table 5). The mass losses observed in the 35–200 °C temperature range, amounting to approximately 7.5% for all samples, are primarily due to the removal of moisture and weakly bound volatile components. Relatively small mass losses (3.74–4.94%) were observed in the range of 200–400 °C, indicating that the majority of the organic components of the raw material, particularly cellulose and hemicellulose, were removed during the pyrolysis of tomato stems [30]. Significant weight loss at high temperatures (600–950 °C) is due to further changes in the carbon structure and the presence of mineral fractions in biochar. The high ash content in the tested samples (Table 6) suggests the involvement of processes occurring in the inorganic phase, which may affect the TG analysis in this temperature range. Total mass losses in the 35–950 °C range decreased with increasing biochar production temperature, from 32.57% for BC400 to 29.06% for BC700. This phenomenon can be attributed to the increasing proportion of the inorganic fraction and to greater transformation of organic material during pyrolysis. Biochars obtained from tomato stems show relatively large mass losses above 600 °C, which is due to their chemical composition. The high ash content (nearly 30% for BC700) and the presence of mineral fractions cause these materials, despite prior thermal treatment, to undergo further significant changes at high temperatures. Similar behavior has been observed in other studies, in which large mass losses at high temperatures were attributed to reactions occurring in the mineral fraction of biochar [31,32]. The presence of this fraction is a consequence of the significant proportion of mineral components in the raw material, amounting to 13.4% (Table 2).

Table 5. Mass loss of biochars obtained from tomato stems determined by thermogravimetric analysis.

Sample	Mass Loss (%)					
	35–200 °C	200–400 °C	400–600 °C	600–800 °C	800–950 °C	35–950 °C
BC400	7.68	4.90	7.13	8.22	4.64	32.57
BC500	7.60	4.94	6.33	8.03	4.25	31.15
BC600	7.56	4.78	6.30	7.63	4.44	30.71
BC700	7.54	3.74	6.09	7.64	4.05	29.06

Table 6. Surface characteristics of tomato stem-derived biochars.

Sample	Iodine Number [mg/g]	Total Acidic Groups (mmol/g)	Total Basic Groups (mmol/g)	Ash Content (wt.%)	Point of Zero Charge (pH_{pzc})
BC400	100	0.269	2.83	23.84	7.65
BC500	105	0.275	3.06	25.05	8.05
BC600	135	0.349	3.89	27.97	8.30
BC700	160	0.385	4.05	29.88	8.65

The results of the Boehm titration (Table 6) indicated a higher concentration of basic functional groups in all biochars (400–700). As the pyrolysis temperature increased, the alkalinity of the biochar surface (total basic groups and pH_{pzc}) also increased. Similar findings were reported by Amer et al. [33]. They found that the pH of tomato stem biochars prepared at 250 °C, 400 °C, and 600 °C were 6.58, 8.38, and 9.23, respectively.

In the case of ash content, one can observe that for increasing temperatures of pyrolysis, it first increases from 400 °C to 600 °C, and then at 700 °C, it decreases.

The iodine number determines the adsorbent's ability to adsorb iodine, directly indicating the textural properties (pore structure, surface area) of the adsorbent. As can be seen, the iodine number increases in the order BC400 < BC500 < BC600 < BC700. This means that BC400 has the lowest specific surface area, while BC700 has the highest. Leng et al. [34] analyzed the effect of pyrolysis temperature on the surface area and porosity of biochar in a review paper. They found that a higher pyrolysis temperature improves porosity and increases the specific surface area of biochars, confirming the results obtained in this study.

The iodine number cannot be directly converted into a specific surface area, but literature data indicate an approximate ratio between the iodine number and specific surface area. Spencer et al. [35] tested various lower-rank Australian coals as precursors for the production of activated carbons. Coals with iodine numbers of 100, 110, and 120 mg/g had specific surface areas of 2.5, 3.6, and 4.0 m^2/g, respectively. Based on these results, we can expect the specific surface area of our biochars, with iodine numbers ranging from 100 to 160 mg/g, to be relatively small. For this reason, nitrogen adsorption–desorption studies were performed only for the BC400 and BC700 biochars, which were prepared under two different temperature conditions. The N_2 adsorption–desorption isotherms for BC400 and BC700 are presented in Figure 2.

The specific surface areas (S_{BET}) of the biochars were calculated using the Brunauer–Emmett–Teller equation. It was found that the BET surface areas were very low, with values of 2.760 m^2/g for BC400 and 4.484 m^2/g for BC700. This finding is consistent with the literature, which reports that the BET surface area of tomato stem-derived biochar produced at 500 °C for 4 h in a N_2 atmosphere was 2.048 m^2/g [16]. Nitrogen isotherms are therefore consistent with the iodine number and confirm the general trend: an increase in biochar surface area with increasing pyrolysis temperature.

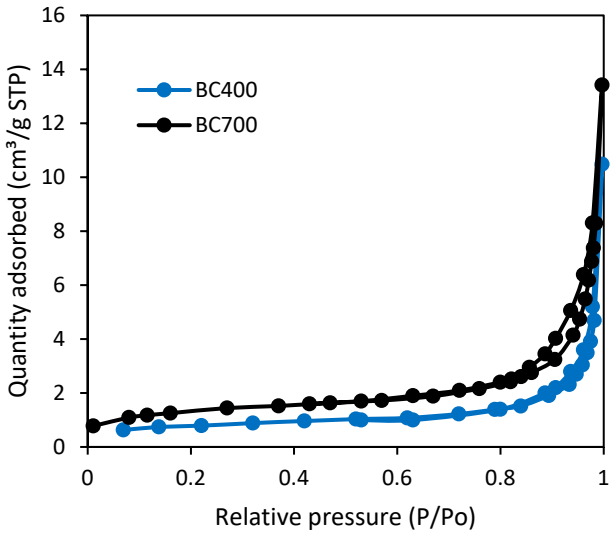

Figure 2. Nitrogen adsorption–desorption isotherm of the BC400 and BC700 samples at 77 K.

The total pore volume and micro- and mesopore volumes were calculated based on the nitrogen isotherm and found to be 0.00444 cm^3/g, 0.00123 cm^3/g, and 0.00321 cm^3/g for BC400 and 0.00714 cm^3/g, 0.00216 cm^3/g, and 0.00498 cm^3/g for BC700, respectively.

3.2. Adsorption Study

3.2.1. Effect of Solution Chemistry

The physicochemical properties of the solution may affect, among other things, the ionization of both the adsorbate and the adsorbent, and thus the overall effectiveness of the adsorption process. Therefore, the effects of pH and ionic strength on the adsorption of both dyes onto biochars derived from tomato stems were evaluated. In this study, the effect of pH was investigated at various pH values (ranging from 2.5 to 10), and the results are presented in Figure 3.

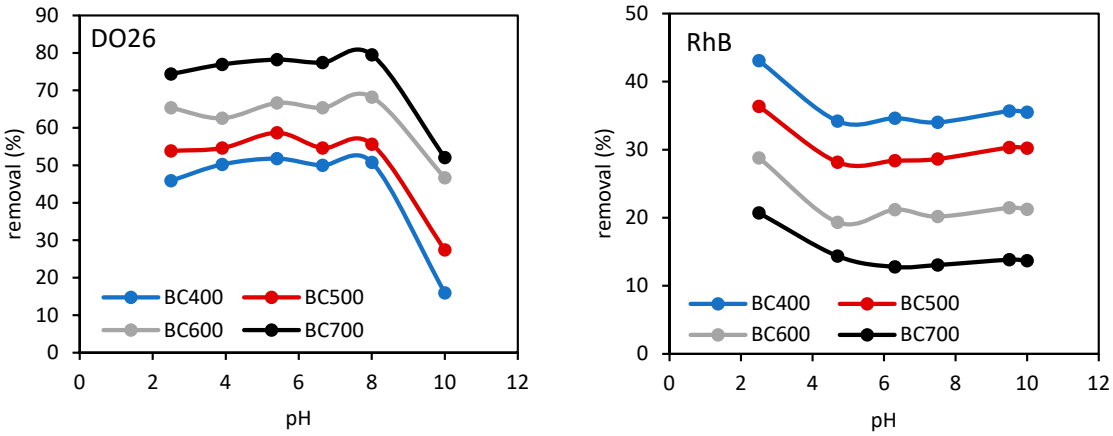

Figure 3. Effect of solution pH on the adsorption of dyes on tomato stem-derived biochars.

The adsorption of DO26 dye remained relatively constant within the pH range of 2.5 to approximately 8.0, after which it decreased sharply, reaching its minimum value in the most alkaline environment at pH 10. Similar results were reported for the adsorption of DO26 onto rice husk [36] and various natural mineral materials [37,38]. This trend was observed in all four biochars, although differences in their adsorption capacities were quite evident. In an acidic environment (pH = 2.5), DO26 was most effectively adsorbed on BC700, with approximately 75% of the dye being removed. This was followed by BC600

(65%), BC500 (54%), and then BC400 (46%), which was the least effective. Increasing the pH of the solution to 10 decreased the adsorption capacities of BC700, BC600, BC500, and BC400 by 29.9%, 26.4%, 18.7%, and 22.3%, respectively.

RhB was also adsorbed most effectively in an acidic environment (pH 2.5). As the pH of the solution increased to around 4–5, adsorption decreased and then stabilized; further increases in the pH of the solution did not cause any additional changes. A similar phenomenon was observed for all four biochars, although their adsorption capacities towards RhB were opposite to those observed for DO26. RhB adsorption was most efficient on BC400 (43%) and least efficient on BC700 (21%). When the pH of the solution increased from 2.5 to 10, a decrease in adsorption efficiency was observed, though this was less evident. Similar findings were also reported for the adsorption of RhB on various natural minerals, including raw and modified halloysites [39], zeolite and chalcedonite [40], activated carbons [41–43], and biochars [44,45].

In the case of adsorbents, their porous structure and surface chemistry play a crucial role in the adsorption process. The physicochemical properties of the biochars tested are discussed in detail in Section 3.1. The specific surface area of the biochars increased with pyrolysis temperature, reaching its maximum value (4.4835 m^2/g) at 700 °C (BC700). The increase in the surface area of biochars corresponds to an increase in DO26 adsorption efficiency (BC400 < BC500 < BC600 < BC700). This suggests that DO26 adsorption depends on the porous structure (i.e., the specific surface area) of biochar. However, given the relatively low surface areas of these adsorbents (a maximum of ~4.5 m^2/g), it seems that their textural properties play a secondary role in practice. The results obtained for RhB also demonstrate that the textural properties of the biochars studied cannot explain their behavior towards cationic dyes. Therefore, it seems that the adsorption of both dyes is more dependent on their surface chemistry than on their porous structure. As shown in Table 6, the alkaline character of the biochar surface increases with increasing pyrolysis temperature, with respective pH_{pzc} values of 7.65, 8.05, 8.30, and 8.65 for BC400, BC500, BC600, and BC700.

In the case of the anionic dye DO26, a positive correlation was observed between biochar alkalinity and dye adsorption. Similar results were reported for the adsorption of other anionic dyes [46]. Faria et al. [46] reported that the presence of acidic surface functional groups reduces the adsorption of anionic dyes. These groups attract electrons, thereby reducing the electron density on the surface of activated carbon and decreasing its affinity for anions. Furthermore, repulsive electrostatic interactions between the anionic dyes and the negatively charged adsorbent surface may enhance this effect.

When it comes to cationic dye adsorption, it's reasonable to expect that these dyes will adsorb onto adsorbents with acidic characteristics. The presence of a greater number of dissociated surface oxygen groups (e.g., carboxyl groups) should promote the uptake of positively charged dyes from water due to the formation of attractive electrostatic interactions between the adsorbate and the adsorbent. Indeed, an analysis of the adsorption capacities of individual biochars as a function of their acid–base properties reveals exactly such a relationship. RhB adsorption was found to be greatest on BC400, the adsorbent with the lowest alkaline character, and lowest on BC700, the most alkaline adsorbent. This suggests that the adsorption of RhB onto tomato stem biochars is primarily due to electrostatic interactions. However, the relationship between adsorption capacity and pH, as observed in Figure 3, negates this conclusion.

Adsorption of dyes is a complex process that can occur through various mechanisms, including electrostatic attraction, π–π interactions between the basal planes of the biochar and the aromatic rings of the dyes, hydrophobic interactions, van der Waals forces, and hydrogen bonding [47]. In the case of DO26 adsorption, electrostatic interactions appear to be

the dominant adsorption mechanism. The anionic dye molecule is preferentially adsorbed in an acidic environment at a pH below the pH_{pzc}, where the surface of the adsorbent is positively charged. The high adsorption efficiency observed under these conditions is therefore the result of attractive electrostatic interactions between the adsorbate and the adsorbent. In an alkaline environment (above pH_{pzc}), negative charges accumulate on the surface of the adsorbent. The significant decrease in DO26 adsorption efficiency observed under these conditions is therefore the result of repulsive electrostatic interactions between the negatively charged dye molecule and the negatively charged surface of the adsorbent. The adsorption behavior of both dyes (Figure 3) suggests different mechanisms for their adsorption onto biochars. If electrostatic attraction were the dominant mechanism of RhB adsorption on biochars, it would occur most preferably in an alkaline environment due to electrostatic attraction between the negatively charged adsorbent surface ($pH > pH_{pzc}$) and the cationic dye molecule. However, the obtained relationship (Figure 3) shows the opposite trend. RhB adsorption was most efficient at pH 2.5 and least efficient at pH 10, indicating that electrostatic adsorbate-adsorbent interactions play a secondary role in adsorption. In this case, π–π and hydrophobic interactions, as well as hydrogen bonding, play a dominant role in the adsorption mechanism.

The findings are in agreement with the observations of other authors who have studied the adsorption of RhB on various biochars [43–45].

The effect of ionic strength on dye adsorption onto biochars was also investigated. Studies were conducted at various NaCl concentrations (0.1, 0.5, 1.0, and 2.0 mol/L), and the results are presented in Figure 4.

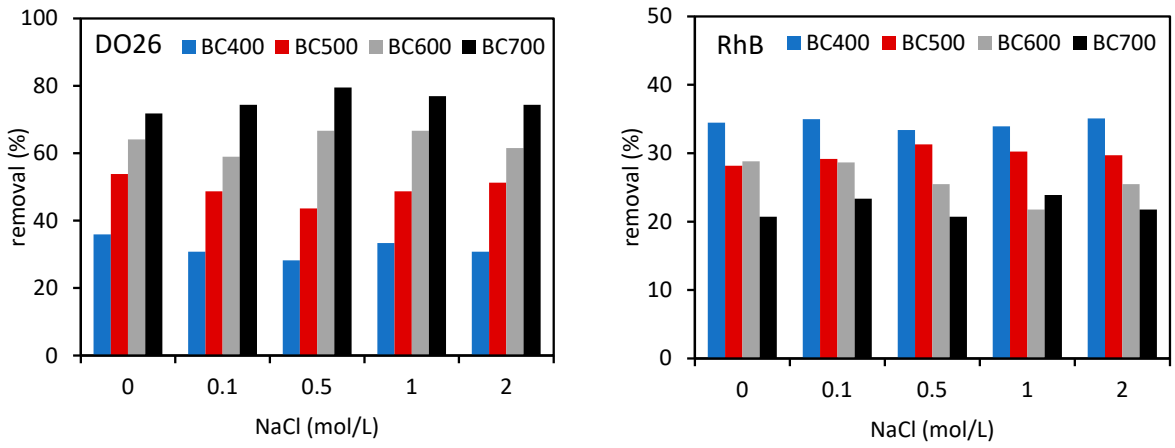

Figure 4. Effect of ionic strength on the adsorption of DO26 and RhB on biochars.

As can be seen, the adsorption efficiency remained constant with increasing inorganic salt concentration in the solution, and the slight fluctuations observed in the plots are likely due to measurement errors instead of actual changes in the adsorption process itself. Therefore, it can be concluded that the adsorption of both dyes onto biochar derived from tomato stems is independent of the ionic strength of the solution. Similar observations were reported previously for the adsorption of DO26 on natural mineral adsorbents [37,38] and the adsorption of RhB on false cypress biomass [48].

3.2.2. Adsorption Kinetics

Adsorption kinetics of DO26 and RhB on tomato stem-derived biochars were investigated at an initial dye concentration of 20 μmol/L and an adsorbent dose of 1 g/L. The results are presented in Figure 5.

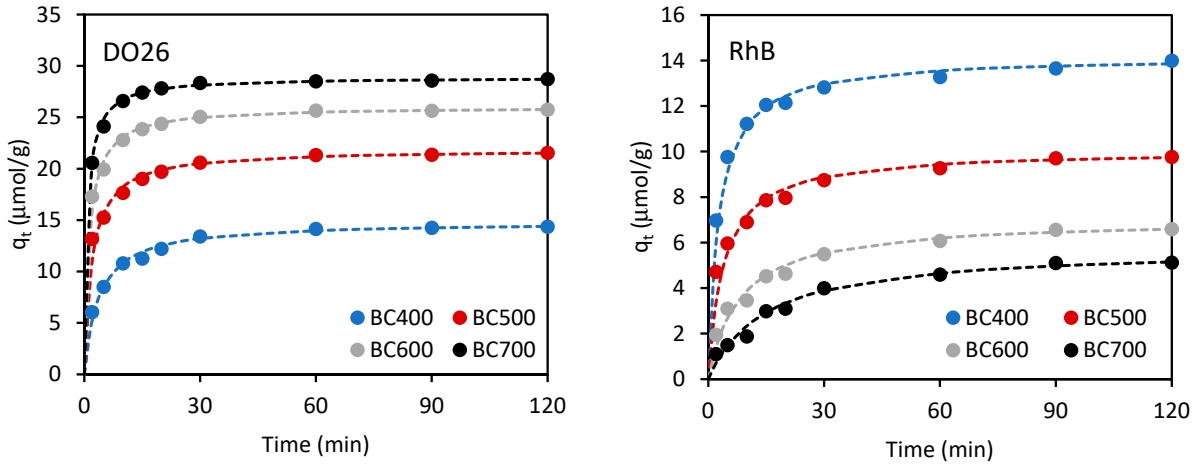

Figure 5. Adsorption kinetics of DO26 and RhB dyes on tomato stem-derived biochars (lines show the fit of the PSO model). Experimental conditions: dye initial concentration = 20 µmol/L, adsorbent dosage = 1 g/L, pH = original (~6.6 for DO26 and ~4.7 for RhB), temperature = 23 °C.

Adsorption equilibrium was achieved after approximately 20–40 min. However, it was difficult to observe the differences between the individual biochars and the dyes. Therefore, to thoroughly analyze the results, the two most popular kinetic models were employed to describe them: the pseudo-first-order (PFO) and pseudo-second-order (PSO) models. The results from the kinetic experiment are shown in Table 7.

Table 7. Kinetic modeling data for the adsorption of the DO26 and RhB dyes on biochars obtained from tomato stems.

Parameter	Biochar			
	BC400	**BC500**	**BC600**	**BC700**
DO26				
$q_{e(exp)}$ (µmol/g)	14.359	21.538	25.744	28.718
pseudo-first-order				
k_1 (1/min)	0.0875	0.0497	0.0737	0.0797
$q_{e(cal)\,1}$ (µmol/g)	13.508	7.485	9.109	8.816
R^2	0.869	0.891	0.915	0.901
χ^2	9.251	8.927	7.298	8.221
RMSE	11.25	10.67	9.261	10.02
pseudo-second-order				
k_2 (g/µmol·min)	0.0182	0.02275	0.02985	0.0421
$q_{e(cal)\,2}$ (µmol/g)	14.837	21.882	26.042	28.902
R^2	0.999	0.998	0.999	0.999
χ^2	0.189	0.498	0.168	0.022
RMSE	0.383	0.794	0.563	0.250
RhB				
$q_{e(exp)}$ (µmol/g)	14.001	9.767	6.596	5.116
pseudo-first-order				
k_1 (1/min)	0.0509	0.0476	0.051	0.0594
$q_{e(cal)\,1}$ (µmol/g)	7.050	5.181	9.368	5.778
R^2	0.879	0.948	0.960	0.923
χ^2	10.21	7.251	6.110	8.201
RMSE	12.231	8.621	7.125	8.992
pseudo-second-order				

Table 7. *Cont.*

Parameter	Biochar			
	BC400	**BC500**	**BC600**	**BC700**
k_2 (g/μmol·min)	0.0251	0.0244	0.0174	0.0117
$q_{e(cal)\,2}$ (μmol/g)	14.184	10.07	7.037	5.787
R^2	0.998	0.999	0.999	0.999
χ^2	0.267	0.653	0.370	0.361
RMSE	0.456	0.516	0.303	0.230

subscript $_1$ comes from pseudo-first-order model; subscript $_2$ comes from pseudo-second-order model.

Significantly higher R^2 values were obtained for the PSO model, as well as lower chi^2 and RMSE values. These results prove that the adsorption of both dyes onto tomato stem biochar follows the pseudo-second-order model. DO26 was adsorbed most slowly on BC400 (k_2 = 0.0182 g/μmol·min) and most quickly on BC700 (k_2 = 0.0421 g/μmol·min). Therefore, the adsorption rate increased with the adsorption capacity and alkalinity of individual biochars. The adsorption rate from aqueous solutions is also affected by the porous structure of the adsorbent. In general, the rate of adsorbate molecule uptake increases with an increase in the number (volume) of mesopores in their structure. This is because mesopores serve as a transport pathway through which adsorbate molecules enter the micropores, where the adsorption process occurs. As discussed in Section 3.1, the mesopore volume of the BC400 and BC7000 biochars was 0.00321 cm^3/g and 0.00498 cm^3/g, respectively.

Zhu et al. [49] studied the effect of thermal treatment of pinewood-derived biochar in the air/nitrogen atmosphere on its porosity. Similar studies on the effect of pyrolysis temperature (600–800 °C) in an air-containing atmosphere on the textural properties of the biochars obtained were published by Li and collaborators [50]. The authors of both studies [49,50] reported that pyrolysis temperature significantly improved the porosity of the biochar, particularly enhancing the development of mesopores. Since the mesopore volume of biochars increases with pyrolysis temperature, one might expect the mesopore volume in these biochars to increase in the order BC400 to BC700, suggesting a positive correlation between mesopore volume and adsorption rate.

Given the low value of mesopore volume of the biochars, the influence of porosity on the kinetics of these materials is likely to be minimal. This is especially true given that the adsorption rate of RhB increases in the opposite order (BC700 < BC600 < BC500 < BC400). These observations demonstrate that the textural properties of the biochars cannot explain their behavior towards anionic (DO26) and cationic (RhB) dyes. The adsorption rate of these dyes depends on the surface chemistry of the biochars and increases (DO26) or decreases (RhB) with increasing their alkaline character.

Although the PSO model accurately describes the adsorption of both dyes on biochars, it does not provide information about the adsorption process itself—its mechanism and the stage that limits the overall rate. Adsorption is a multi-stage process consisting of (1) diffusion of the adsorbate through the boundary layer, (2) diffusion of adsorbate molecules in the pores of the adsorbent, and (3) surface reaction between the adsorbate and adsorbent [20]. The last stage happens almost immediately, so the adsorption rate is determined by its slowest stage—film diffusion or interparticle (pore) diffusion.

The Weber–Morris kinetic model [20,21] may help solve this problem. Based on the q_t versus $t^{0.5}$ plot, this model identifies the stage of adsorption that determines the overall process rate. There are four possible situations: (1) the plot of $q_t = f(t^{0.5})$ is linear; (2) the plot is not a straight line; (3) the plot passes through the origin; and (4) the plot does not pass through the origin. Depending on the situation, this means that (1) the adsorption rate is controlled by one step only—either film diffusion or pore diffusion; (2) adsorption is

more complex, and both stages control the adsorption rate; (3) intraparticle diffusion is the primary rate-limiting step in adsorption; and (4) pore diffusion plays a secondary role, and the adsorption rate is controlled by film diffusion.

Figure 6 shows the Weber–Morris kinetics for DO26 and RhB. The kinetic curves are broken and do not start at the origin. This suggests that the adsorption of both dyes onto tomato stem-derived biochars is a complex process, where the adsorption rate is affected by both film diffusion and pore diffusion. However, film diffusion is the rate-limiting step that controls the overall adsorption process.

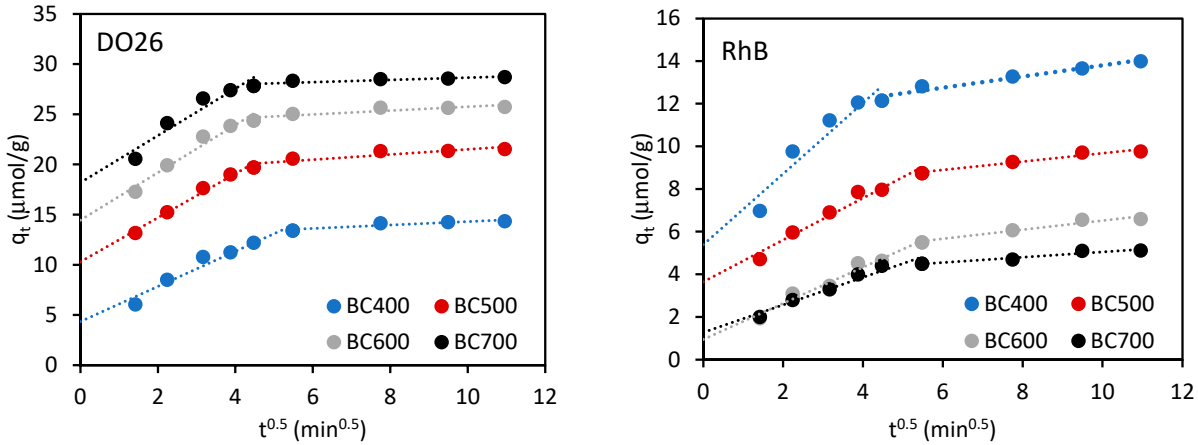

Figure 6. The Weber–Morris diffusion model plots for the adsorption of DO26 and RhB on tomato stem-derived biochars.

3.2.3. Adsorption Isotherm

Figure 7 shows the adsorption isotherms of both dyes on the tested biochars.

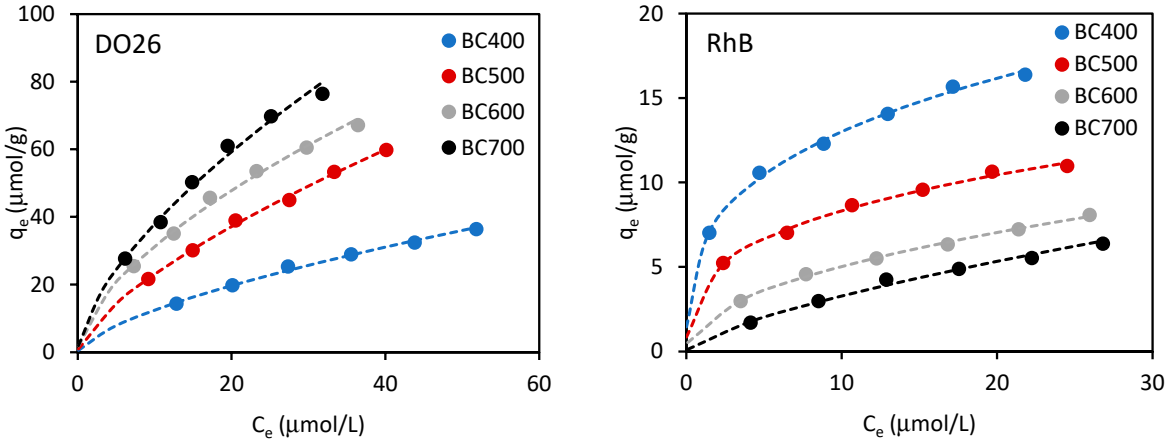

Figure 7. Adsorption isotherms of DO26 and RhB dyes on tomato stem-derived biochars (lines show the fit of the Freundlich model). Experimental conditions: dye initial concentration = 20–70 µmol/L for DO2620 and 5–30 µmol/L for RhB µmol/L, adsorbent dosage = 1 g/L, pH = original (~6.6 for DO26 and ~4.7 for RhB), temperature = 23 °C.

The Freundlich, Langmuir, and Temkin isotherm models were used to describe the experimental data [22], and the results are presented in Table 8.

Table 8. Adsorption isotherm parameters for the adsorption of DO26 and RhB on tomato stem-derived biochars.

Parameter	Biochar			
	BC400	**BC500**	**BC600**	**BC700**
DO26				
Freundlich				
K_F ((μmol/g)·(L/μmol)$^{1/n}$)	2.724	4.717	7.646	8.633
$1/n$	0.660	0.689	0.612	0.643
R^2	0.995	0.997	0.994	0.992
χ^2	0.034	0.076	0.114	0.232
RMSE	0.402	0.733	0.824	1.292
Langmuir				
q_m (μmol/g)	71.94	116.3	126.6	142.8
K_L (L/μmol)	0.019	0.021	0.037	0.038
R^2	0.991	0.971	0.990	0.981
χ^2	0.079	0.166	0.193	0.371
RMSE	0.581	1.081	1.273	1.902
Temkin				
b_T (kJ/mol)	0.158	0.096	0.094	0.080
A_T (L/g)	0.186	0.231	0.335	0.361
R^2	0.951	0.977	0.941	0.963
χ^2	0.274	0.672	0.664	1.017
RMSE	0.669	1.228	1.529	2.130
RhB				
Freundlich				
K_F ((μmol/g)·(L/μmol)$^{1/n}$)	6.273	3.901	1.637	0.653
$1/n$	0.316	0.329	0.487	0.701
R^2	0.996	0.995	0.997	0.991
χ^2	0.024	0.018	0.100	0.045
RMSE	0.222	0.165	0.093	0.180
Langmuir				
q_m (μmol/g)	18.55	12.90	10.98	9.360
K_L (L/μmol)	0.290	0.215	0.092	0.038
R^2	0.990	0.991	0.977	0.983
χ^2	0.483	0.230	0.081	0.152
RMSE	0.783	0.456	0.263	0.205
Temkin				
b_T (kJ/mol)	0.708	0.967	1.004	1.055
A_T (L/g)	4.568	2.882	0.866	0.440
R^2	0.986	0.982	0.976	0.983
χ^2	0.087	0.043	0.074	0.165
RMSE	0.261	0.213	0.138	0.201

Analyzing the R^2, χ^2, and RMSE values obtained for individual isotherms reveals that all three models generally describe the adsorption of dyes onto biochars quite well. However, slightly higher R^2 values and lower χ^2 and RMSE values were obtained for the Freundlich model.

To confirm the Freundlich equation as the best fit, a mass balance method was used [51]. According to the assumptions of this method, the following relationship should be satisfied for a constant solution volume:

$$C_0 = C_e + C_e^S \quad (20)$$

where C_0 is the initial adsorbate concentration, C_e is the concentration of adsorbate remaining in the solution after equilibrium is reached, and C_e^S is the concentration of adsorbate adsorbed onto the surface of the adsorbent. Taking into account the mass balance in Freundlich's equation and performing a further transformation yields the following relationships:

$$\frac{K_F m}{V} C_e^{1/n} + C_e - C_0 = 0 \quad (21)$$

$$C_0 - \left(\frac{m}{V} K_F C_e^{\frac{1}{n}} \right) = C_e \quad (22)$$

These equations enable the determination of the value of C_e. The C_e values obtained in this way, after substitution into Equation (5), allow for the calculation of the value of $q_{e\,CAL}$. The plot of $q_{e\,CAL}$ versus the experimental values of q_e ($q_{e\,EXP}$) is shown in Figure 8.

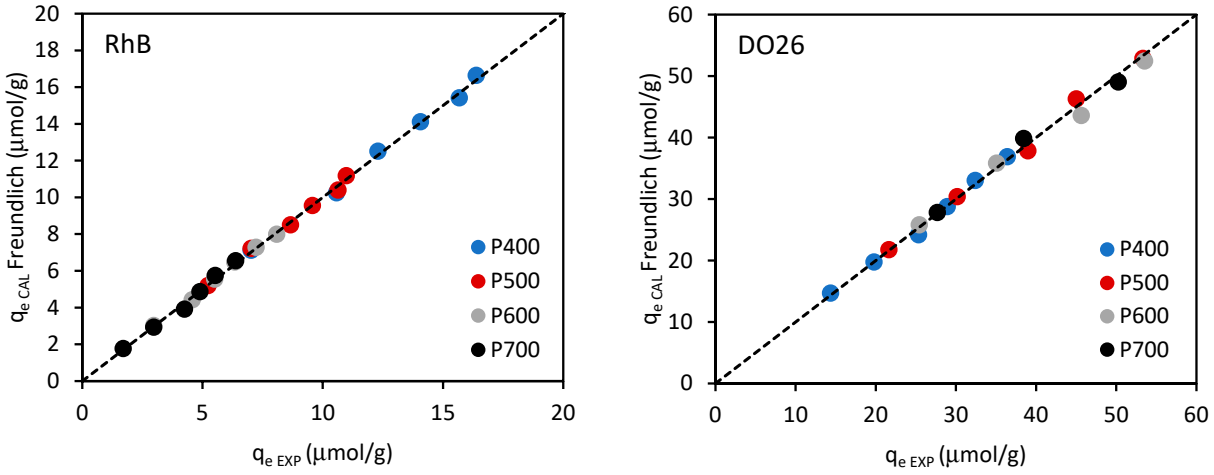

Figure 8. Linear regression plots of the experimental ($q_{e\,EXP}$) and predicted adsorption capacity ($q_{e\,CAL}$) calculated using the Freundlich model.

The results show a strong correlation between the experimental and calculated data for all biochars, confirming that the adsorption of both dyes follows the Freundlich isotherm model. It can therefore be concluded that the Freundlich model provides a better description of the multilayer adsorption of DO26 and RhB by the biochars, indicating interactions between the dye molecules and the heterogeneous nature of the adsorbent's surface.

Analyzing the constants shown in Table 8, it can be concluded that DO26 was adsorbed most preferably on BC700 and least efficiently on BC400. For RhB, however, the opposite order can be observed. As discussed in Section 3.2.1, the adsorption of both dyes was more dependent on the biochar surface chemistry than on its textural properties. Adsorption of the anionic dye increased, and adsorption of the cationic dye decreased with increasing alkalinity of the adsorbent surface. Isothermal studies were conducted at the original pH of the RhB (~4.7) and DO26 (~6.6) solutions. The dominant mechanism of DO26 adsorption was therefore electrostatic interactions, whereas for RhB, it was a combination of π–π and hydrophobic interactions, as well as H-bonding.

For a complete evaluation of the potential of tomato stem biochars, their adsorption capacities for the tested adsorbates should be compared with those of other materials described in the literature. Tables 9 and 10 present such a comparison for DO26 and RhB, respectively. For standardization, all adsorption capacities were converted and presented as milligrams per gram of adsorbent. As can be seen in Table 8, biochars obtained from tomato stems are characterized by a very good (better than most adsorbents described in the literature) ability to remove DO26. The adsorption capacities of biochars from tomato stems toward RhB are slightly lower but still satisfactory (Table 9). Their adsorption capacities

are better than those obtained for biochar derived from *Pongamia glabra* seed cover [52] or biochar from groundnut husk [43], comparable to mineral adsorbents, and significantly weaker than those reported for activated carbons and other biochars. This demonstrates that tomato stem-derived biochars are a promising and cost-effective adsorbent for removing anionic and cationic dyes from water.

Table 9. Adsorption isotherm parameters for the adsorption of DO26 and RhB on tomato stem-derived biochars.

Adsorbent	Adsorption Capacity (mg/g)	Ref.
BC400	54.44	this study
BC500	87.98	this study
BC600	95.78	this study
BC700	108.1	this study
hard coal	13.80	[38]
lignite	15.10	[38]
peat	17.70	[38]
rice husk	19.96	[36]
Lignin–ZnO composite	45.01	[53]
HCl-modified rice husk	46.98	[43]
raw halloysite	49.13	[37]
Ficus nano zero-valent copper	98.04	[54]
H_2SO_4-treated halloysite	290.6	[37]

Table 10. Adsorption isotherm parameters for the adsorption of DO26 and RhB on tomato stem-derived biochars.

Adsorbent	Adsorption Capacity (mg/g)	Ref.
BC400	8.887	this study
BC500	6.018	this study
BC600	5.258	this study
BC700	4.483	this study
biochar from *Pongamia glabra* waste	0.683	[52]
biochar from groundnut husk	2.379	[44]
ultrasound-treated halloysite	4.010	[39]
activated carbon from stalk corn	5.300	[55]
H_2SO_4-treated halloysite	6.290	[39]
biomass of false cypress	6.830	[48]
zeolite	6.964	[40]
Fe–N biochar	12.41	[56]
Spartina alterniflora biochar	28.14	[43]
biochar from tapioca peel waste	33.10	[57]
activated tire pyrolysis char (AC110)	33.52	[41]
activated tire pyrolysis char (AC150)	63.94	[41]
Samanea saman waste pods carbon	101.0	[42]
modified pine nut shell biochar	110.7	[58]
biochar from cotton straw	117.8	[45]

4. Conclusions

This study demonstrated the effectiveness of biochars obtained through the pyrolysis of tomato stems at various temperatures (400–700 °C) in removing anionic (Direct Orange 26) and cationic (Rhodamine B) dyes from aqueous solutions. The BCs (400–700) were characterized using, inter alia, scanning electron microscopy (SEM) with energy-dispersive X-ray analysis (EDX), thermogravimetry (TG), Boehm titration, and N_2 adsorption–desorption isotherm analysis. The characterization of BCs and the adsorption studies revealed that the process is mainly governed by the surface chemistry of biochars rather than their textural properties. The adsorption of anionic dyes increased, while that of cationic dyes decreased, as the alkalinity of the adsorbent surface increased. The ability of BCs to adsorb DO26 is due to electrostatic attraction, while the adsorption of RhB was rather a result of π–π and hydrophobic interactions and hydrogen bonding. Adsorption of both dyes was found to be pH-dependent, but no effect of ionic strength was observed. Kinetic analysis revealed that the pseudo-second-order model best describes the adsorption process, indicating that film diffusion was the rate-limiting step. The Freundlich model provided the best fit for the equilibrium data, indicating multilayer adsorption of the dyes on a heterogeneous surface of BCs. The maximum adsorption capacities of BCs range from 54.44 to 108.1 mg/g for DO26 and from 4.483 to 8.887 mg/g for RhB. Adsorption capacities increased for DO26 and decreased for RhB as the pyrolysis temperature and alkalinity of the biochar surfaces increased. Overall, tomato stem-derived biochars demonstrated promising potential as cost-effective adsorbents for removing anionic and cationic dyes from water.

Author Contributions: Conceptualization: B.D., K.K. and A.Ś.; methodology: B.D., K.K. and A.Ś.; formal analysis and investigation: B.D., K.K. and A.Ś.; preparation and characterization of activated carbons: B.D.; adsorption processes and their analysis: K.K. and A.Ś.; writing—original draft preparation: B.D., K.K. and A.Ś.; writing—review and editing: B.D.; visualization: K.K.; resources: B.D., K.K. and A.Ś.; supervision: A.Ś. All authors have read and agreed to the published version of the manuscript.

Funding: This research received no external funding.

Institutional Review Board Statement: Not applicable.

Informed Consent Statement: Not applicable.

Data Availability Statement: The original contributions presented in this study are included in the article. Further inquiries can be directed to the corresponding author.

Acknowledgments: The authors of this paper would like to thank all those who contributed to the realization of this work.

Conflicts of Interest: The authors declare no conflicts of interest.

References

1. Li, P.; Zhao, T.; Zhao, Z.; Tang, H.; Feng, W.; Zhang, Z. Biochar Derived from Chinese Herb Medicine Residues for Rhodamine B Dye Adsorption. *ACS Omega* **2023**, *8*, 4813–4825. [CrossRef] [PubMed]
2. Eskikaya, O.; Arslan, H.; Gun, M.; Bouchareb, R.; Dizge, N. Adsorption of Direct Orange 46 and phosphate ions on waste tomato stem ash used as a bio-based adsorbent. *Environ. Prog. Sustain. Energy* **2023**, *42*, e14192. [CrossRef]
3. Srivatsav, P.; Bhargav, B.H.; Shanmugasundaram, V.; Arun, J.; Gopinath, K.P.; Bhatnagar, A. Biochar as an Eco-Friendly and Economical Adsorbent for the Removal of Colorants (Dyes) from Aqueous Environment: A Review. *Water* **2020**, *12*, 3561. [CrossRef]
4. Ahmed, S.F.; Mehejabin, F.; Chowdhury, A.A.; Almomani, F.; Khan, N.A.; Badruddin, I.A.; Kamangar, S. Biochar produced from waste-based feedstocks: Mechanisms, affecting factors, economy, utilization, challenges, and prospects. *GCB Bioenergy* **2024**, *16*, e13175. [CrossRef]

5. Laishram, D.; Kim, S.-B.; Lee, S.-Y.; Park, S.-J. Advancements in Biochar as a Sustainable Adsorbent for Water Pollution Mitigation. *Adv. Sci.* **2025**, *12*, 2410383. [CrossRef]
6. Santos, D.C.B.D.; Evaristo, R.B.W.; Dutra, R.C.; Suarez, P.A.Z.; Silveira, E.A.; Ghesti, G.F. Advancing Biochar Applications: A Review of Production Processes, Analytical Methods, Decision Criteria, and Pathways for Scalability and Certification. *Sustainability* **2025**, *17*, 2685. [CrossRef]
7. Leng, L.; Huang, H. An overview of the effects of pyrolysis process parameters on biochar stability. *Bioresour. Technol.* **2018**, *270*, 627–642. [CrossRef]
8. Rex, P.; Mohammed Ismail, K.R.; Meenakshisundaram, N.; Barmavatu, P.; Sai Bharadwaj, A.V.S.L. Agricultural Biomass Waste to Biochar: A Review on Biochar Applications Using Machine Learning Approach and Circular Economy. *Chem. Eng.* **2023**, *7*, 50. [CrossRef]
9. Kabir, E.; Kim, K.-H.; Kwon, E.E. Biochar as a tool for the improvement of soil and environment. *Front. Environ. Sci.* **2023**, *11*, 1324533. [CrossRef]
10. Tan, X.; Liu, Y.; Zeng, G.; Wang, X.; Hu, X.; Gu, Y.; Yang, Z. Application of biochar for the removal of pollutants from aqueous solutions. *Chemosphere* **2015**, *125*, 70–85. [CrossRef]
11. Haris, M.; Amjad, Z.; Usman, M.; Saleem, A.; Dyussenova, A.; Mahmood, Z.; Dina, K.; Guo, J.; Wang, W. A review of crop residue-based biochar as an efficient adsorbent to remove trace elements from aquatic systems. *Biochar* **2024**, *6*, 47. [CrossRef]
12. Yaashikaa, P.R.; Senthil Kumara, P.; Sunita, V.; Saravanand, A. A critical review on the biochar production techniques, characterization, stability and applications for circular bioeconomy. *Biotechnol. Rep.* **2020**, *28*, e00570. [CrossRef] [PubMed]
13. Drescher, A.; Schwingshack, L.; Kienberger, M. Identification of molecules from tomato plant residues using sustainable green chemicals. *Biomass Convers. Biorefin.* **2025**, *15*, 14387–14398. [CrossRef]
14. Tiryaki, B.; Yagmur, E.; Banford, A.; Aktas, Z. Comparison of activated carbon produced from natural biomass and equivalent chemical compositions. *J. Anal. Appl. Pyrolysis.* **2014**, *105*, 276–283. [CrossRef]
15. Szymańska, J.; Doczekalska, B.; Strzemiecka, B.; Bednarek, W.H.; Woźniak, M.; Paukszta, D. Polypropylene composites with biochars from miscanthus and tomato biomass, Part I: Thermal and Structural Properties. *J. Nat. Fibers.* **2023**, *20*, 2282047. [CrossRef]
16. Gkiliopoulos, D.; Pemas, S.; Torofias, S.; Triantafyllidis, K.; Bikiaris, D.N.; Terzopoulou, Z.; Pechlivani, E.M. Valorization of Tomato Stem Waste: Biochar as a Filler in Three-Dimensional Printed PLA Composites. *Polymers* **2025**, *17*, 2565. [CrossRef]
17. Seifert, K. Zur Frage der Cellulose-Schnellbestimmung nach der Acetylaceton-Methode. *Das Papier* **1960**, *14*, 104–106.
18. Boehm, H.P. Surface oxides on carbon and their analysis: A critical assessment. *Carbon* **2002**, *40*, 145–149. [CrossRef]
19. *D4607-14*; Standard Test Method for Determination of Iodine Number of Activated Carbon. ASTM International: West Conshohocken, PA, USA, 2021. [CrossRef]
20. Tan, K.L.; Hameed, B.H. Insight into the adsorption kinetics models for the removal of contaminants from aqueous solutions. *J. Taiwan Inst. Chem.* **2017**, *74*, 25–48. [CrossRef]
21. Nasser, S.M.; Abbas, M.; Trari, M. Understanding the Rate-Limiting Step Adsorption Kinetics onto Biomaterials for Mechanism Adsorption Control. *Prog. React. Kinet. Mech.* **2024**, *49*, 1–26. [CrossRef]
22. Al-Ghouti, M.A.; Da'ana, D.A. Guidelines for the use and interpretation of adsorption isotherm models: A review. *J. Hazard. Mater.* **2020**, *393*, 122383. [CrossRef] [PubMed]
23. Fengel, D.; Wegener, G. *Wood: Chemistry, Ultrastructure, Reactions*; Walter de Gruyter: Berlin, Germany, 1989; ISBN 3-11-012059-3.
24. Sjöström, E. *Wood Chemistry: Fundamentals and Applications*; Academic Press: San Diego, CA, USA, 1993; ISBN 0-12-647481-8.
25. Rowell, R.M. *Handbook of Wood Chemistry and Wood Composites*; CRC Press: Boca Raton, FL, USA, 2012.
26. Doczekalska, B.; Bartkowiak, M.; Waliszewska, B.; Orszulak, G.; Cerazy-Waliszewska, J.; Pniewski, T. Characterization of chemically activated carbons prepared from miscanthus and switchgrass biomass. *Materials* **2020**, *13*, 1654. [CrossRef] [PubMed]
27. Coimbra, M.C.; Duque, A.; Saez, F.; Manzanares, P.; Garcia-Cruz, C.H.; Ballesteros, M. Sugar production from wheat straw biomass by alkaline extrusion and enzymatic hydrolysis. *Renew. Energy* **2016**, *86*, 1060–1068. [CrossRef]
28. Gupta, A.; Kataria, P.; Sharma, V. Physical, chemical composition and morphological analysis of rice husk reinforced epoxy composites. *Oxf. Open Mater. Sci.* **2025**, *5*, itaf012. [CrossRef]
29. Ayala-Cortés, A.; Arancibia-Bulnes, C.A.; Villafán-Vidales, H.I.; Lobato-Peralta, D.R.; Martínez-Casillas, D.C.; Cuentas-Gallegos, A.K. Solar pyrolysis of agave and tomato pruning wastes: Insights of the effect of pyrolysis operation parameters on the physicochemical properties of biochar. *AIP Conf. Proc.* **2019**, *2126*, 180001. [CrossRef]
30. Li, S.; Chen, G. Thermogravimetric, thermochemical, and infrared spectral characterization of feedstocks and biochar derived at different pyrolysis temperatures. *Waste Manag.* **2018**, *78*, 198–207. [CrossRef]
31. Li, B.; Liu, D.; Lin, D.; Xie, X.; Wang, S.; Xu, H.; Wang, J.; Huang, Y.; Zhang, S.; Hu, X. Changes in Biochar Functional Groups and Its Reactivity after Volatile−Char Interactions during Biomass Pyrolysis. *Energy Fuels* **2020**, *34*, 14291–14299. [CrossRef]

32. Puri, L.; Hu, Y.; Naterer, G. Critical review of the role of ash content and composition in biomass pyrolysis. *Front. Fuels* **2024**, *2*, 1378361. [CrossRef]
33. Amer, A.E.; El-Desoky, M.A.; El-Eyuoon, A.; Amin, A.; Farrag, H.M. Effects of Pyrolysis Temperatures of Tomato Stems Biochar on Soil Properties and Nitrogen Use Efficiency of Wheat Plant Grown in Sandy Soil. *Assiut J. Agri. Sci.* **2024**, *55*, 197–215. [CrossRef]
34. Leng, L.; Xiong, Q.; Yang, L.; Li, H.; Zhou, Y.; Zhang, W.; Jiang, S.; Li, H.; Huang, H. An overview on engineering the surface area and porosity of biochar. *Sci. Total Environ.* **2021**, *763*, 144204. [CrossRef]
35. Spencer, W.; Ibana, D.; Singh, P.; Nikoloski, A.N. Effect of Surface Area, Particle Size and Acid Washing on the Quality of Activated Carbon Derived from Lower Rank Coal by KOH Activation. *Sustainability* **2024**, *16*, 5876. [CrossRef]
36. Safa, Y.; Bhatti, H.N. Kinetic and thermodynamic modeling for the removal of Direct Red-31 and Direct Orange-26 dyes from aqueous solutions by rice husk. *Desalination* **2011**, *272*, 313–322. [CrossRef]
37. Kuśmierek, K.; Świątkowski, A.; Wierzbicka, E.; Legocka, I. Enhanced adsorption of Direct Orange 26 dye in aqueous solutions by modified halloysite. *Physicochem. Probl. Miner. Process.* **2020**, *56*, 693–701. [CrossRef]
38. Kuśmierek, K.; Dąbek, L.; Świątkowski, A. Removal of Direct Orange 26 azo dye from water using natural carbonaceous materials. *Arch. Environ. Prot.* **2023**, *49*, 47–56. [CrossRef]
39. Wierzbicka, E.; Kuśmierek, K.; Świątkowski, A.; Legocka, I. Efficient Rhodamine B Dye Removal from Water by Acid- and Organo-Modified Halloysites. *Minerals* **2022**, *12*, 350. [CrossRef]
40. Kuśmierek, K.; Fronczyk, J.; Świątkowski, A. Adsorptive removal of Rhodamine B dye from aqueous solutions using mineral materials as low-cost adsorbents. *Water Air Soil Pollut.* **2023**, *234*, 531. [CrossRef]
41. Kuśmierek, K.; Świątkowski, A.; Kotkowski, T.; Cherbański, R.; Molga, E. Adsorption of Rhodamine B from water by activated char obtained from end-of-life tyre pyrolysis. *Chem. Process Eng.* **2023**, *44*, e1. [CrossRef]
42. Kumbhar, P.; Patil, S.; Narale, D.; Sartape, A.; Jambhale, C.; Kim, J.-H.; Kolekar, S. Biobased carbon for effective removal of rhodamine B and Cr(VI) from aqueous solution: Kinetic, isotherm and thermodynamic study. *Biomass Convers. Biorefin.* **2024**, *14*, 3535–3550. [CrossRef]
43. Yu, W.; Xie, Z.; Zhang, N.; Tang, L.; Xia, J.; Ye, J.; Liu, X.; Wang, D.; Yang, G. Sustainable optimization of high specific surface area Spartina alterniflora biochar for Rhodamine B removal and mechanism. *Sci. Rep.* **2025**, *15*, 21745. [CrossRef]
44. Kayranli, B. Adsorption efficiency of groundnut husk biochar in reduction of rhodamine B, recycle, and reutilization. *Biomass Convers. Biorefin.* **2025**, *15*, 25501–25513. [CrossRef]
45. dos Santos, T.P.M.; Dias, B.M.; Sousa, H.M.; de Menezes Filho, F.C.M.; Fukumoto, A.A.F.; da Cruz, I.F.; de Morais, E.B. Adsorption of rhodamine B onto cotton straw-derived biochar: Kinetic, equilibrium, thermodynamics, and predictive studies using artificial intelligence. *Int. J. Phytoremediat.* **2025**, *27*, 1913–1925. [CrossRef] [PubMed]
46. Faria, P.C.C.; Órfão, J.J.M.; Pereira, M.F.R. Adsorption of anionic and cationic dyes on activated carbons with different surface chemistries. *Water Res.* **2004**, *38*, 2043–2052. [CrossRef] [PubMed]
47. Dutta, S.; Gupta, B.; Srivastava, S.K.; Gupta, A.K. Recent advances on the removal of dyes from wastewater using various adsorbents: A critical review. *Mater. Adv.* **2021**, *2*, 4497–4531. [CrossRef]
48. Gul, S.; Gul, H.; Gul, M.; Khattak, R.; Rukh, G.; Khan, M.S.; Aouissi, H.A. Enhanced Adsorption of Rhodamine B on Biomass of Cypress/False Cypress (*Chamaecyparis lawsoniana*) Fruit: Optimization and Kinetic Study. *Water* **2022**, *14*, 2987. [CrossRef]
49. Zhu, X.; Li, C.; Li, J.; Xie, B.; Lü, J.; Li, Y. Thermal treatment of biochar in the air/nitrogen atmosphere for developed mesoporosity and enhanced adsorption to tetracycline. *Bioresour. Technol.* **2018**, *263*, 475–482. [CrossRef]
50. Li, C.; Zhu, X.; He, H.; Fang, Y.; Dong, H.; Lü, J.; Li, J.; Li, Y. Adsorption of two antibiotics on biochar prepared in air-containing atmosphere: Influence of biochar porosity and molecular size of antibiotics. *J. Mol. Liq.* **2019**, *274*, 353–361. [CrossRef]
51. Chung, H.-K.; Kim, W.-H.; Park, J.; Cho, J.; Jeong, T.-Y.; Park, P.-K. Application of Langmuir and Freundlich isotherms to predict adsorbate removal efficiency or required amount of adsorbent. *J. Ind. Eng. Chem.* **2015**, *28*, 241–246. [CrossRef]
52. Bordoloi, N.; Dey, M.D.; Mukhopadhyay, R.; Kataki, R. Adsorption of Methylene blue and Rhodamine B by using biochar derived from Pongamia glabra seed cover. *Water Sci. Technol.* **2018**, *77*, 638–646. [CrossRef]
53. Sajjad, A.; Aftab, K.; Siddique, Z.; Khan, M.R.; Khan, M.A.; Kausar, A.; Ahmad, N.; Baig, M.A.; Wahab, R. Eco-friendly removal of direct orange 26 dye using lignin-ZnO composite: Optimization and application. *J. Environ. Manag.* **2025**, *388*, 125927. [CrossRef]
54. Abd El-Aziz, H.M.; Zayed, M.A.; Abdel-Gawad, S.A. Adsorptive removal of Direct Red 31 and Direct Orange 26 azo dyes from aqueous solutions using Ficus nano zero valent copper: Linear, non-linear, response surface methodology (RSM), and artificial neural network (ANN) modeling. *Adsorpt. Sci. Technol.* **2024**, *42*, 1–24. [CrossRef]
55. Mousavi, S.A.; Kamarehie, B.; Almasi, A.; Darvishmotevalli, M.; Salari, M.; Moradnia, M.; Azimi, F.; Ghaderpoori, M.; Neyazi, Z.; Karami, M.A. Removal of Rhodamine B from aqueous solution by stalk corn activated carbon: Adsorption and kinetic study. *Biomass Convers. Biorefin.* **2023**, *13*, 7927–7936. [CrossRef]
56. Li, X.; Shi, J.; Luo, X. Enhanced adsorption of rhodamine B from water by Fe-N co-modified biochar: Preparation, performance, mechanism and reusability. *Bioresour. Technol.* **2022**, *343*, 126103. [CrossRef]

57. Vigneshwaran, S.; Sirajudheen, P.; Karthikeyan, P.; Meenakshi, S. Fabrication of sulfur-doped biochar derived from tapioca peel waste with superior adsorption performance for the removal of Malachite green and Rhodamine B dyes. *Surf. Interf.* **2021**, *23*, 100920. [CrossRef]
58. Eroğlu, H.A.; Kadıoğlu, E.N.; Akbal, F. High-efficiency removal of Rhodamine B using modified biochar from agricultural waste pine nut shell: Investigation of kinetics, isotherms, and artificial neural network modeling. *Biomass Convers. Biorefin.* **2025**, *15*, 12137–12150. [CrossRef]